DELFT UNIVERSITY OF TECHNOLOGY

REPORT 94-24

Finite volume computation of 2D incompressible turbulent flows in general coordinates on staggered grids

M. Zijlema, A. Segal and P. Wesseling

ISSN 0922-5641

Reports of the Faculty of Technical Mathematics and Informatics no. 94-24

Delft 1994

Abstract

A brief review of some publications on computation of incompressible turbulent flow in complex geometries is given. A 2D finite volume method for the calculation of turbulent flow in general curvilinear coordinates is described. This method is based on a staggered grid arrangement and the contravariant flux components are chosen as primitive variables. Turbulence is modeled by the standard k-ε model with wall functions. Applications of this method to a variety of flows are presented. The results of computations are compared with experimental data and other numerical solutions and are found to be satisfactory.

1 Introduction

Solving incompressible turbulent flows using a boundary-fitted coordinate system is an important technique in CFD. It permits an easy and accurate implementation of boundary conditions and makes the computation of flows in complex geometries possible. For this purpose two different approaches can be adopted. The first approach is a complete transformation of the Navier-Stokes equations to general coordinates. Such a coordinate-invariant formulation contains many geometric quantities and thus leads to more work and storage. Moreover, the equations involve Christoffel symbols which may lead to inaccuracies on non-smooth grids. Another approach is a partial transformation, in which only the independent variables are transformed while retaining the velocity components as Cartesian components. As a result, the governing equations have a strong conservation form which has a much simpler structure and thus simplifies programming of codes.

The choice of the two approaches mentioned above depends on a grid arrangement: staggered versus colocated. On staggered grids one may choose Cartesian velocity components as unknowns in the Navier-Stokes equations, because of simplicity. But these velocity components, in general, are not perpendicular to grid lines. Therefore, this approach may lead to unstable discretization. Hence, the choice of grid-oriented velocity components as dependent variables is preferable. On colocated grids Cartesian velocity components as primitive variables in the momentum equations are satisfactory.

In order to compute turbulent flows a turbulence model has to be chosen. Many investigators adopt isotropic eddy-viscosity formulations, of which a k-ε model is the

most prominent. This model consists of two transport equations for the turbulent kinetic energy k and its dissipation rate ε. Both equations contain a quantity P_k called the production rate of turbulent energy. In the coordinate-invariant approach this quantity contains Christoffel symbols (in 2D eight different Christoffel symbols occur). Hence, it seems attractive to implement the k-ε model with the Cartesian approach.

In the light of the above observations, the colocated/Cartesian approach for solving the Reynolds-averaged Navier-Stokes equations with the k-ε model has become very popular and has been widely used over the last 15 years [Habib and Whitelaw, 1982], [Rhie and Chow, 1983], [Perić, 1985], [Chen and Patel, 1989], [Deng, 1989], [Piquet and Queutey, 1990], [Lien and Leschziner, 1991], [Cho and Fletcher, 1991], [Melaaen, 1991], [Coelho and Pereira, 1992], [Zhu and Rodi, 1992], [Xu *et al.*, 1993], [Rolfes *et al.*, 1993] and [Issa and Oliveira, 1994].

Within the colocated approach the pseudo-compressibility method can also be used. This has been done e.g. in [Kwak *et al.*, 1986] and [V. Michelassi and F. Martelli, 1990]. The former used an algebraic eddy-viscosity model while the latter used the k-ε model. The main disadvantage of this method is that for time-dependent flow problems it is difficult to obtain accurate mass conservation.

Although the colocated approach is very popular, an important disadvantage of this approach is that there are special measures required to obtain a stable discretization (for example the Rhie and Chow interpolation to avoid decoupling between pressure and velocity).

Staggered grid arrangement has important advantages for incompressible flow computations, because this arrangement avoids non-physical pressure oscillations. Some publications discretizing the Reynolds-averaged Navier-Stokes equations for staggered grids with Cartesian velocity components as primitive variables including the k-ε model in general coordinates are [Rapley, 1985], [Braaten and Shyy, 1986], [Yung *et al.*, 1989] and [Chen *et al.*, 1990]. It should be recognized that this approach may give rise to unstable discretizations. Following Chen *et al.* (1990), the more common way to avoid this, is to choose the coordinate system such that the angle between the velocity components and the grid lines is not too large. However, for special domains it is very difficult to achieve this, especially in 3D.

Discretizations for staggered grids with grid-oriented velocity components as unknowns with the k-ε model are presented in [Pope, 1978], [Rastogi, 1984], [Demirdzic *et al.*, 1987], [Stern *et al.*, 1988], [Majumdar and Rodi, 1989] and [Koshizuka and Oka, 1991]. Stern *et al.* (1988) have formulated the governing equations in vector notation which has the advantage that Christoffel symbols do not occur explicitly. Rastogi (1984) and Majumdar *et al.* (1989) use contravariant velocity components to solve the Navier-Stokes equations, while Pope (1978), Demirdzic *et al.* (1987) and Koshizuka *et al.* (1991) employ contravariant physical velocity components as unknowns.

In [Mynett *et al.*, 1991], [Wesseling *et al.*, 1992] and [Segal *et al.*, 1992] a coordinate-invariant discretization of the incompressible Navier-Stokes equations on a general staggered grid has been developed. Standard tensor notation has been used. As a consequence, the formulation contains Christoffel symbols. In spite of that, discretization accuracy can be maintained if certain rules concerning the

approximation of the geometric quantities are followed and the contravariant flux components are chosen as primitive variables, and the grid is not too non-smooth. Good results are obtained for 2D laminar flows on fairly smooth grids.

In this paper a finite volume method for turbulent flow predictions on staggered grids in complex geometries employing the contravariant flux components as dependent variables is presented. Turbulence is modeled by the standard high-Re k-ε model with wall functions. The discretization incorporates central differences for the momentum equations and hybrid central/upwind differences for the turbulence equations. Accurate approximation of production of turbulent energy (defined in (2.13)) is obtained. The method is applied to some complex 2D turbulent recirculating flows, namely driven cavity flow, flow over a backward facing step, constricted tube flow and flow through an U-bend.

2 Equations governing incompressible turbulent flows in general coordinates

In order to formulate the equations governing turbulent flow in general coordinates, tensor notation will be used; for an introduction see [Aris, 1962].

The physical domain with curved boundaries Ω is transformed to a rectangle G with the mapping

$$T : \boldsymbol{x} = \boldsymbol{x}(\boldsymbol{\xi}), \quad \boldsymbol{x} \in \Omega, \boldsymbol{\xi} \in G \tag{2.1}$$

Here, $\boldsymbol{x}$ are Cartesian coordinates and $\boldsymbol{\xi}$ are boundary conforming curvilinear coordinates. The mapping is assumed to be regular, i.e. the Jacobian of the transformation does not vanish. Covariant base vectors $\boldsymbol{a}_{(\alpha)}$, contravariant base vectors $\boldsymbol{a}^{(\alpha)}$, and the covariant and contravariant metric tensors $g_{\alpha\beta}$ and $g^{\alpha\beta}$ are defined as

$$\boldsymbol{a}_{(\alpha)} = \frac{\partial \boldsymbol{x}}{\partial \xi^\alpha}, \quad \boldsymbol{a}^{(\alpha)} = \frac{\partial \xi^\alpha}{\partial \boldsymbol{x}}, \quad g_{\alpha\beta} = \boldsymbol{a}_{(\alpha)} \cdot \boldsymbol{a}_{(\beta)}, \quad g^{\alpha\beta} = \boldsymbol{a}^{(\alpha)} \cdot \boldsymbol{a}^{(\beta)} \tag{2.2}$$

The square root of the determinant of the covariant metric tensor, denoted by $\sqrt{g}$, equals the Jacobian of the transformation. The following formulae for covariant derivatives of tensors of rank zero, one and two, respectively, are used in this paper:

$$\phi_{,\alpha} = \frac{\partial \phi}{\partial \xi^\alpha} \tag{2.3}$$

$$U^\alpha_{,\beta} = \frac{\partial U^\alpha}{\partial \xi^\beta} + \{ {}^{\alpha}_{\gamma\beta} \} U^\gamma \tag{2.4}$$

$$U^\alpha_{,\alpha} = \frac{1}{\sqrt{g}} \frac{\partial \sqrt{g} U^\alpha}{\partial \xi^\alpha} \tag{2.5}$$

$$T^{\alpha\beta}_{,\beta} = \frac{1}{\sqrt{g}} \frac{\partial \sqrt{g} T^{\alpha\beta}}{\partial \xi^\beta} + \{ {}^{\alpha}_{\gamma\beta} \} T^{\gamma\beta} \tag{2.6}$$

where

$$\{ {}^{\alpha}_{\gamma\beta} \} = \boldsymbol{a}^{(\alpha)} \cdot \frac{\partial \boldsymbol{a}_{(\beta)}}{\partial \xi^\gamma} = \frac{\partial \xi^\alpha}{\partial x^\delta} \cdot \frac{\partial^2 x^\delta}{\partial x^\gamma \partial \xi^\beta} = \{ {}^{\alpha}_{\beta\gamma} \} \tag{2.7}$$

is the Christoffel symbol of the second kind. The summation convention holds for Greek indices.

Turbulent flow is governed by the continuity equation and the Reynolds-averaged Navier-Stokes equations. The Reynolds stresses are related to the mean rates of strain through the isotropic eddy-viscosity ν_t, which is calculated by the standard high-Re k-ε model [Launder and Spalding, 1974]. The tensor formulation of these equations is given by

$$U^{\alpha}_{,\alpha} = 0 \tag{2.8}$$

$$\frac{\partial U^{\alpha}}{\partial t} + (U^{\alpha}U^{\beta})_{,\beta} + (g^{\alpha\beta}p)_{,\beta} - ((\nu+\nu_t)(g^{\alpha\gamma}U^{\beta}_{,\gamma} + g^{\beta\gamma}U^{\alpha}_{,\gamma}))_{,\beta} = F^{\alpha} \tag{2.9}$$

$$\nu_t = c_{\mu}\frac{k^2}{\varepsilon} \tag{2.10}$$

$$\frac{\partial k}{\partial t} + (U^{\alpha}k)_{,\alpha} - (\frac{\nu_t}{\sigma_k}g^{\alpha\beta}k_{,\beta})_{,\alpha} = P_k - \varepsilon \tag{2.11}$$

$$\frac{\partial \varepsilon}{\partial t} + (U^{\alpha}\varepsilon)_{,\alpha} - (\frac{\nu_t}{\sigma_{\varepsilon}}g^{\alpha\beta}\varepsilon_{,\beta})_{,\alpha} = \frac{\varepsilon}{k}(c_{\varepsilon 1}P_k - c_{\varepsilon 2}\varepsilon) \tag{2.12}$$

where U^{α} is the contravariant mean velocity component, p is the pressure, ν is the kinematic viscosity, F^{α} is an external force per unit volume, k is the turbulent kinetic energy, ε is the turbulent energy dissipation rate and P_k is the production of turbulent energy, given by

$$P_k = \nu_t g_{\alpha\delta}(g^{\alpha\gamma}U^{\beta}_{,\gamma} + g^{\beta\gamma}U^{\alpha}_{,\gamma})U^{\delta}_{,\beta} \tag{2.13}$$

Finally, c_{μ}, $c_{\varepsilon 1}$, $c_{\varepsilon 2}$, σ_k and σ_{ε} are dimensionless constants which, respectively, are taken to be 0.09, 1.44, 1.92, 1.0 and 1.3. The values of these constants are recommended in [Launder and Spalding, 1974].

Specification of the boundary conditions is straightforward, except in near-wall regions where wall functions are adopted to avoid integration through the viscous sublayer and to obtain log-layer solutions [Launder and Spalding, 1974]. These wall functions are given by:

$$\tau_w = \begin{cases} \nu\dfrac{\boldsymbol{u}\cdot\boldsymbol{t}}{Y}, & Y^+ < 11.3 \\ \dfrac{c_{\mu}^{1/4}\kappa\sqrt{k}}{\ln(EY^+)}\boldsymbol{u}\cdot\boldsymbol{t}, & Y^+ \geq 11.3 \end{cases} \tag{2.14}$$

where

$$Y^+ = \frac{c_{\mu}^{1/4}Y\sqrt{k}}{\nu} \tag{2.15}$$

and

$$P_k = \tau_w\frac{\boldsymbol{u}\cdot\boldsymbol{t}}{Y} \tag{2.16}$$

$$\varepsilon = \begin{cases} c_{\mu}^{3/4}k^{3/2}\dfrac{Y^+}{Y}, & Y^+ < 11.3 \\ c_{\mu}^{3/4}k^{3/2}\dfrac{\ln(EY^+)}{\kappa Y}, & Y^+ \geq 11.3 \end{cases} \tag{2.17}$$

Here, τ_w is the wall shear stress, Y is the distance perpendicular to the wall, κ is the Von Kármán constant (≈ 0.4) and E is a roughness parameter, approximately equal to 9.0 for a smooth wall. The quantity $\boldsymbol{u} \cdot \boldsymbol{t}$ denotes the tangential velocity along the wall and is given by

$$\boldsymbol{u} \cdot \boldsymbol{t} = \frac{g_{t\alpha}}{\sqrt{g_{tt}}} U^\alpha, \quad t = 1 \text{ or } 2 \tag{2.18}$$

Finally, the flux of turbulent energy through the wall is set to zero and the value of ε at the first grid point away from the wall is determined from

$$\varepsilon = \frac{c_\mu^{3/4} k^{3/2}}{\kappa Y} \tag{2.19}$$

3 Discretization of the governing equations

3.1 Invariant finite volume discretization

In discretizing the governing equations (2.8)-(2.12), the following requirements should be met for accuracy reasons:

1. The geometric identity $\oint a_\beta^{(\alpha)} d\Gamma_\alpha = 0$ should be satisfied after discretization.
2. When representing a constant velocity field $\boldsymbol{u}$ in terms of its contravariant components U^α, and recomputing $\boldsymbol{u}$ from U^α, the original vector field $\boldsymbol{u}$ should be recovered exactly.

The first requirement imposes rules on the approximation of geometric quantities. The second requirement can be met if the flux components $V^\alpha = \sqrt{g} U^\alpha$ are chosen as unknowns. More details can be found in [Mynett *et al.*, 1991], [Wesseling *et al.*, 1992] and [Segal *et al.*, 1992].

A finite volume method is used to discretize the governing equations on a staggered grid in the computational rectangle G. In G we choose a uniform grid, choosing the mapping $\boldsymbol{x} = \boldsymbol{x}(\boldsymbol{\xi})$ such that the mesh-size $\delta\xi^\alpha = 1$. Figure 3.1 shows the locations of the points for the velocities U^α and pressure p in the grid. The turbulence

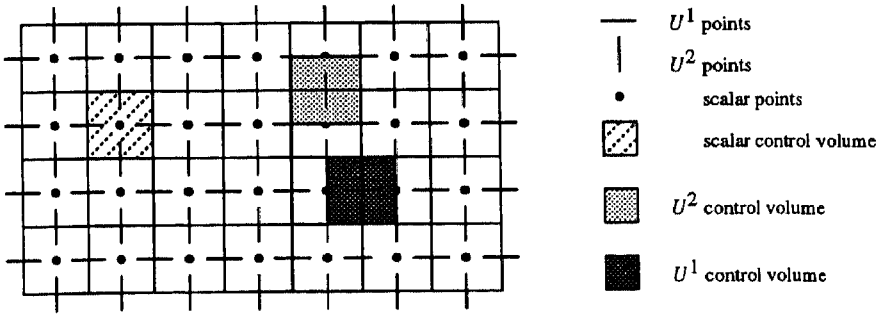

Figure 3.1: Arrangement of the unknowns for a staggered grid

quantities k and ε are evaluated at pressure points. For brevity the momentum and k-ε equations are written in the following form:

$$T^{\alpha\beta}_{,\beta} = F^{\alpha} - \frac{\partial U^{\alpha}}{\partial t} \tag{3.1}$$

where

$$T^{\alpha\beta} = U^{\alpha}U^{\beta} + g^{\alpha\beta}p - (\nu + \nu_t)(g^{\alpha\gamma}U^{\beta}_{,\gamma} + g^{\beta\gamma}U^{\alpha}_{,\gamma}) \tag{3.2}$$

and

$$Q^{\alpha}_{,\alpha} = S_{\phi} - \frac{\partial \phi}{\partial t} \tag{3.3}$$

where

$$Q^{\alpha} = U^{\alpha}\phi - \frac{\nu_t}{\sigma_{\phi}} g^{\alpha\beta}\phi_{,\beta} \tag{3.4}$$

Here, $\phi = k$ or ε and S_{ϕ} represents the nonlinear source terms. For convenience we introduce the local cell coordinates given by Figure 3.2.

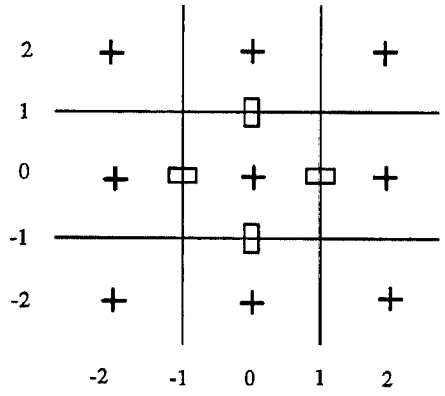

Figure 3.2: Local cell coordinates

Discretization of the continuity equation is obtained by integration over a finite volume Ω with center (0,0), using (2.5):

$$\int_{\Omega} U^{\alpha}_{,\alpha} d\Omega = \int_{\Omega} \frac{\partial \sqrt{g} U^{\alpha}}{\partial \xi^{\alpha}} d\xi^1 d\xi^2 \approx V^1|^{(1,0)}_{(-1,0)} + V^2|^{(0,1)}_{(0,-1)} = 0 \tag{3.5}$$

The momentum equation (3.1) is discretized in space as follows, taking for example a U^1-cell with center at (1,0), using (2.6):

$$\begin{aligned} \int_{\Omega} T^{1\beta}_{,\beta} d\Omega &= \int_{\Omega} \frac{\partial \sqrt{g} T^{1\beta}}{\partial \xi^{\beta}} d\xi^1 d\xi^2 + \int_{\Omega} \{^{1}_{\gamma\beta}\} T^{\gamma\beta} \sqrt{g} d\xi^1 d\xi^2 \\ &\approx \sqrt{g} T^{11}|^{(2,0)}_{(0,0)} + \sqrt{g} T^{12}|^{(1,1)}_{(1,-1)} + \sqrt{g} \{^{1}_{\gamma\beta}\} T^{\gamma\beta}|_{(1,0)} \end{aligned} \tag{3.6}$$

Integration of the momentum equation with $\alpha = 2$ over a U^2-cell with center (0,1) is done similarly.

Using (2.5), the transport equation (3.3) is integrated over a pressure cell with center (0,0) which yields

$$\int_{\Omega} Q^{\alpha}_{,\alpha} d\Omega \approx \sqrt{g} Q^1|^{(1,0)}_{(-1,0)} + \sqrt{g} Q^2|^{(0,1)}_{(0,-1)} \tag{3.7}$$

The right-hand sides of (3.1) and (3.3) are integrated using midpoint rules:

$$\int_\Omega (F^\alpha - \frac{\partial U^\alpha}{\partial t}) d\Omega \approx \sqrt{g}_{(k,l)} (F^\alpha - \frac{\partial U^\alpha}{\partial t})|_{(k,l)} \tag{3.8}$$

and

$$\int_\Omega (S_\phi - \frac{\partial \phi}{\partial t}) d\Omega \approx \sqrt{g}_{(0,0)} (S_\phi - \frac{\partial \phi}{\partial t})|_{(0,0)} \tag{3.9}$$

with $(k,l) = (1,0)$ if $\alpha = 1$ or $(k,l) = (0,1)$ if $\alpha = 2$.

The discretization is completed by substituting (3.2) in (3.6) and (3.4) in (3.7). Furthermore, U^α is replaced by $V^\alpha/\sqrt{g}$. The cell-face fluxes containing cell-face values (convection) and derivatives (diffusion) have to be approximated. Central differences will be employed, except for the convection of turbulence equations in which a hybrid central/upwind scheme [Spalding, 1972] will be adopted. The reason for this is as follows. The k-ε equations are highly nonlinear and coupled. As a consequence, the computational task is complicated, because numerical experiments have shown that the convergence of iterative methods, to solve this coupled nonlinear problem, is adversely affected by negative values of k and ε which occur when convection is approximated by a non-positive (e.g. central) scheme. Using the hybrid scheme, the approximation of the face value ϕ at point (1,0), for example, is given by

$$\phi_{(1,0)} = \{1 - s(Pe^1_{(1,0)})\}\phi_C + s(Pe^1_{(1,0)})\phi_U \tag{3.10}$$

where ϕ_C and ϕ_U are given by

$$\phi_C = \frac{1}{2}(\phi_{(0,0)} + \phi_{(2,0)}) \tag{3.11}$$

$$\phi_U = \frac{1}{2}\{1 + sign(V^1_{(1,0)})\}\phi_{(0,0)} + \frac{1}{2}\{1 - sign(V^1_{(1,0)})\}\phi_{(2,0)} \tag{3.12}$$

Furthermore, the mesh-Péclet number $Pe^\alpha_{(k,l)}$ is defined by

$$Pe^\alpha_{(k,l)} = \frac{\sigma_\phi V^\alpha_{(k,l)}}{2\nu_t \sqrt{g}_{(k,l)} g^{\alpha\alpha}_{(k,l)}}, \quad \text{no summation over } \alpha \tag{3.13}$$

If $|Pe^\alpha_{(k,l)}| > 1$, a first order upwind scheme is used, otherwise a switch to central differences is applied. The switching function $s(Pe)$ is defined as

$$s(Pe) = \begin{cases} 0, & |Pe| \leq 1.0 \\ 1, & |Pe| > 1.0 \end{cases} \tag{3.14}$$

Non-orthogonal coordinates introduce mixed derivatives in diffusion terms, which make the scheme non-positive even when upwind discretization is applied. Many authors (e.g. Rhie and Chow (1983), Demirdzic *et al.* (1987) and Melaaen (1991)) treat these derivatives in an explicit manner, i.e. calculating them from values obtained in the previous iteration, but we found that our iterative solver allows to treat the mixed derivatives implicitly. Nonetheless, in some circumstances (highly non-orthogonal grid or large non-alignment of grid lines and streamlines) this scheme

may produce numerical instability. In such cases certain precautions will have to be taken; for a discussion see [Zijlema, 1993].

The discretization of the production of turbulent energy (2.13) is carried out by substituting (2.4) in (2.13) and with central differencing. Again, U^α is replaced by $V^\alpha/\sqrt{g}$. In spite of the presence of Christoffel symbols numerical experiments have shown that this discretization gives good results on reasonable smooth grids.

The discretization of the V^1-momentum equation results in the 19-point stencil presented in Figure 3.3. The V^2 stencil is obtained by rotation over 90°. The total

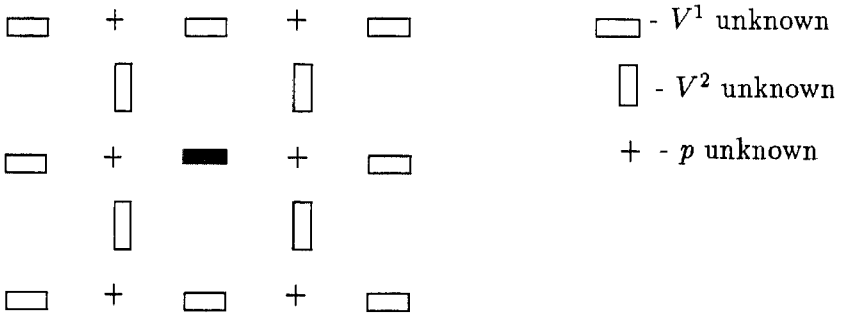

Figure 3.3: Stencil for V^1-momentum equation

number of variables linked together in the transport equation is 9.

Implementation of boundary conditions for the momentum and transport equations is discussed in [Segal *et al.*, 1992] and [Zijlema, 1993]. Also discussion about the implementation of periodic as well as antiperiodic boundary conditions in our code can be found in [Segal *et al.*, 1993].

3.2 Time discretization and solution method

The spatial discretization yields systems of ordinary differential equations of the following form:

$$DV = \boldsymbol{O} \tag{3.15}$$

$$\frac{d\boldsymbol{V}}{dt} + N(\boldsymbol{V}) + G\boldsymbol{P} = \boldsymbol{F} \tag{3.16}$$

$$\frac{d\boldsymbol{\phi}}{dt} + T(\boldsymbol{V})\boldsymbol{\phi} = \boldsymbol{B} + \boldsymbol{S}_\phi \tag{3.17}$$

where $\boldsymbol{V}$, $\boldsymbol{P}$ and $\boldsymbol{\phi}$ denote algebraic vectors containing the velocity, pressure and scalar unknowns, respectively. Furthermore, D and G are the discretized divergence and gradient operators, N and T represent the discretization of convection and diffusion terms, $\boldsymbol{F}$ contains the discretized source term and boundary values, $\boldsymbol{B}$ represents a right-hand side term arising from the boundary conditions and $\boldsymbol{S}_\phi$ contains the source term which is a function of $\boldsymbol{V}$ and $\boldsymbol{\phi}$. Time discretization takes place with the implicit Euler method. Linearization of nonlinear terms is carried out with the standard Newton method:

$$N(\boldsymbol{V}^{n+1}) \approx N(\boldsymbol{V}^n) + \frac{\partial N^n}{\partial \boldsymbol{V}}(\boldsymbol{V}^{n+1} - \boldsymbol{V}^n) \tag{3.18}$$

and

$$S_\phi^{n+1} \approx S_\phi^n + \frac{\partial S_\phi^n}{\partial \phi}(\phi^{n+1} - \phi^n) \tag{3.19}$$

For both the k and ε equations the inequalities $S_\phi^n \geq 0$ and $\partial S_\phi^n / \partial \phi < 0$ hold, which preserves positivity of the solutions. For a derivation see [Zijlema, 1993]. The resulting systems of linear equations are solved by a Krylov subspace method of GMRES type [Saad and Schultz, 1986] with preconditioning. This method is very suitable for non-symmetric matrices, has a relatively good rate of convergence, and is vectorizable to a satisfactory degree. For more details we refer to [Vuik, 1993]. Most authors, like Rapley (1985), Demirdzic *et al.* (1987), Majumdar and Rodi (1989), Melaaen (1991) and Coelho and Pereira (1992) adopted more slowly convergent iterative methods for solving the momentum and turbulence equations, of which the line Gauss-Seidel method and the strongly implicit method of Stone (1968) are the most prominent. Both iterative methods are only partly vectorizable.

The overall solution algorithm can be summarized as follows: first, the continuity equation and the momentum equations are solved. To ensure a divergence-free velocity field a second order pressure-correction method as described by Van Kan (1986) is used. Details can be found e.g. in [Segal *et al.*, 1992]. Finally, the equations for k and ε are solved in a decoupled way. Time-stepping is repeated until a stationary solution is obtained.

4 Results

In this section applications of the present method to 2D turbulent flows, both geometrically and physically complex, are described. Only flow situations that are well documented in the literature will be investigated. These include flows in a driven cavity, over a backward facing step, through a constricted tube and through an U-bend.

4.1 Driven cavity flow

The calculation of a driven cavity flow shown in Figure 4.1 is compared with the ex-

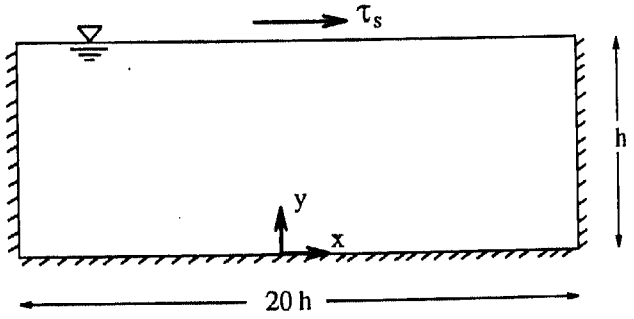

Figure 4.1: The domain for the driven cavity flow (not to scale)

periments of Baines and Knapp (1965). Furthermore, experimental data for the velocity along the vertical plane in the middle of the cavity are taken from [Rodi, 1984].

At walls, the wall functions are applied. At the moving wall the experimental surface shear stress τ_s is given. In order to reduce the turbulence length scale near the moving wall, the following boundary conditions for k and ε are used:

$$k = \frac{u_{\tau_s}^2}{\sqrt{c_\mu}}, \qquad \varepsilon = \frac{u_{\tau_s}^3}{\kappa y} \tag{4.1}$$

where $u_{\tau_s} \equiv \sqrt{\tau_s/\rho}$ is the surface friction velocity and y is the distance perpendicular to the moving wall. The Reynolds number based on the surface friction velocity and the depth h of the cavity is approximately 6,000.

Figure 4.2 shows the 80x50 mesh in which the grid cells are highly stretched in

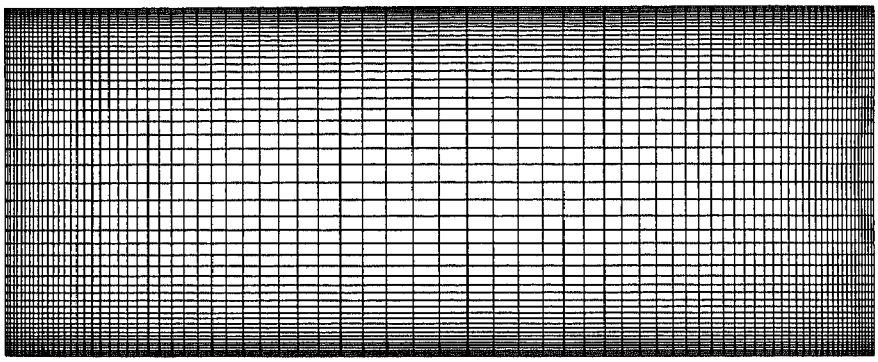

Figure 4.2: Grid used for prediction of flow in driven cavity (not to scale)

order to resolve the steep velocity gradients near the walls.

The predicted normalized velocity profile along the vertical plane in the middle of the cavity is shown and compared with the experimental data in Figure 4.3. It is

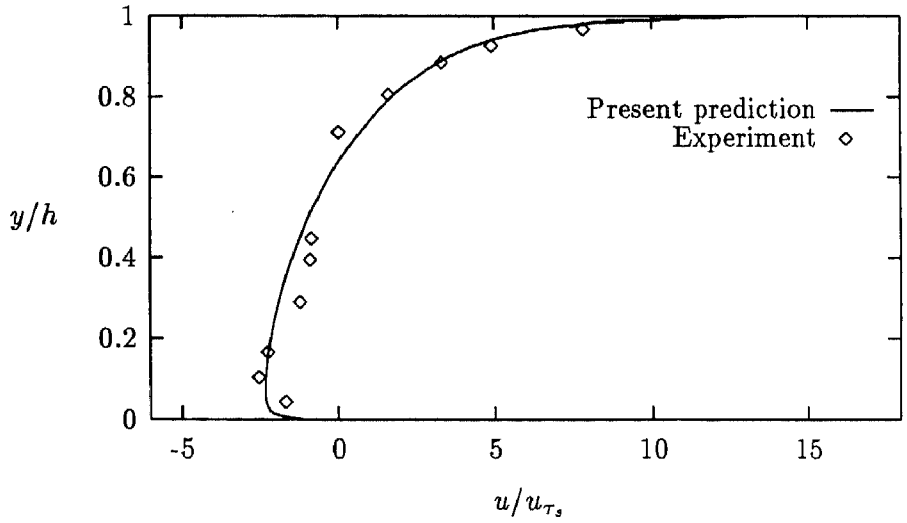

Figure 4.3: Streamwise velocity profile at $x = 0.0$ m

seen that the calculation is in very good agreement with the measurements. Hence, it may be concluded that this type of flows are well described by the standard k-ε

model. Furthermore, our general coordinate discretization is accurate on the non-uniform grid of Figure 4.2. Convergence of the preconditioned GMRES method was not adversely affected by the high (up to 10) mesh aspect ratios which occur.

4.2 Turbulent flow over a backward facing step

Turbulent flow over a backward facing step is a widely used benchmark problem to evaluate the performance of turbulence models in the prediction of separated flows. It is well-known that the standard k-ε model with wall functions underpredicts the reattachment length in the backward facing step by an amount in the order of 20-25%. This has been widely discussed since the 1980-81 AFOSR-HTTM Stanford Conference on Complex Turbulent Flows, see e.g. [Demirdzic, 1982], [Nallasamy, 1987] and [Thangam and Speziale, 1991].

In this section we present some results. For the computations the flow configuration of [Kim *et al.*, 1980] (which was one of the test cases in the aforementioned conference) has been selected. In this case the ratio of step height to outlet channel height is 1:3 and the Reynolds number based on the step height and U_0 is 44,000. The domain is sketched in Figure 4.4.

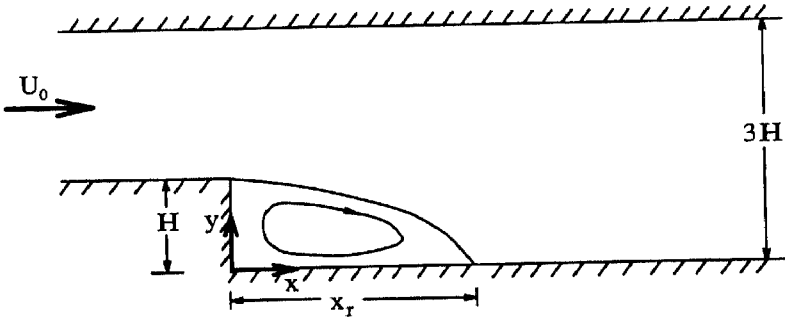

Figure 4.4: Geometry of the backward facing step flow

Inlet profiles for velocities and turbulence quantities are specified at 4 step heights upstream of the step corner. These profiles are obtained from a preliminary calculation of a fully developed turbulent flow in a straight channel for the given Reynolds number. Wall functions are used at the upper and lower walls and outstream conditions (i.e. normal stress and tangential velocity are zero and zero normal gradient conditions for turbulence quantities) are applied 30 step heights downstream of the step.

Figure 4.5 shows a part of the non-orthogonal 40x94 mesh employed. Overall, the mesh is smooth except near the step. In fact, the backward facing step problem is suited for a multiblock approach in which an orthogonal coordinate system can be employed. However, our purpose is to test our general coordinates discretization. Inaccuracies will occur with the present grid, which will be shown later. An initial calculation with a 20x45 grid indicates little change in the reattachment length compared to the result from the 40x94 grid. Hence, further grid refinement seems unnecessary.

In Figure 4.6 the computed streamlines are shown. The calculated reattachment

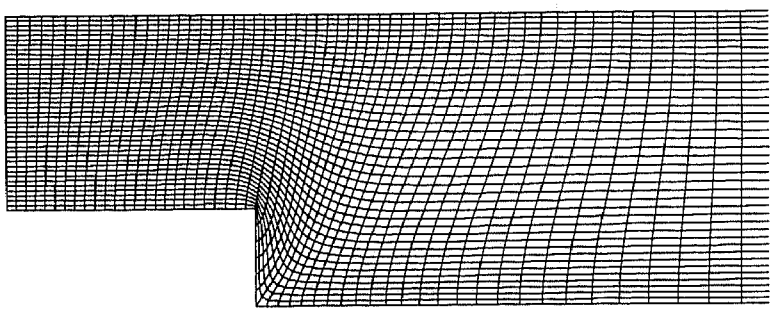

Figure 4.5: A part of the 40x94 grid for the backward facing step flow

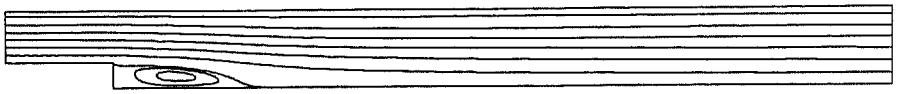

Figure 4.6: Predicted streamlines for flow over the backward facing step

length is $x_r/H = 5.3$, which gives 24% underprediction of the experimental reattachment length of $x_r/H \approx 7$. This result resembles the results found earlier at the aformentioned conference very well. Plots of calculated isobars, turbulence intensity (defined as $\sqrt{k}/U_0$) and turbulence length scale (defined as $c_\mu k^{3/2}/\varepsilon H$) are shown in Figure 4.7.

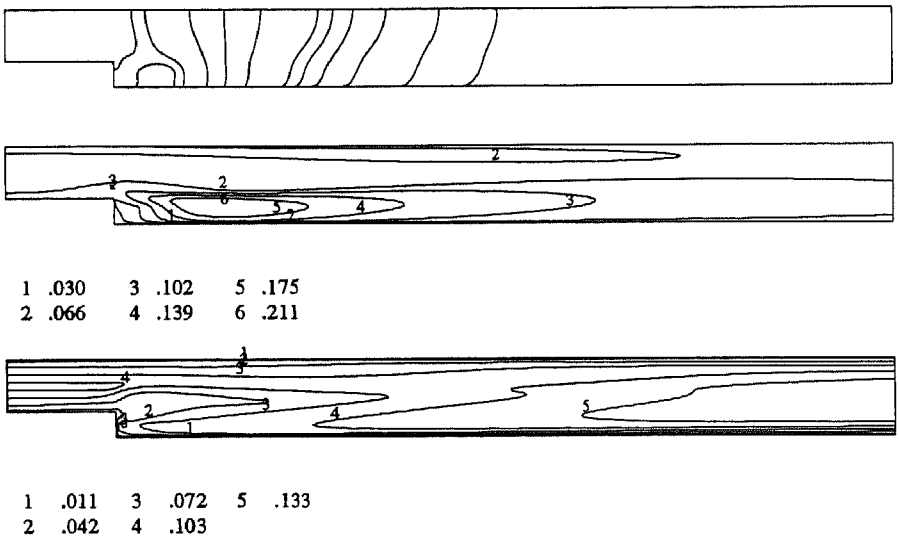

Figure 4.7: Predicted features of turbulent flow over the backward facing step: isobars, turbulence intensity and length scales, respectively

Profiles of the normalized streamwise velocity are given in Figures 4.8, 4.9 and 4.10 and are compared with the experimental data. As can be seen, there is reasonably good agreement between the computations and the experimental results and

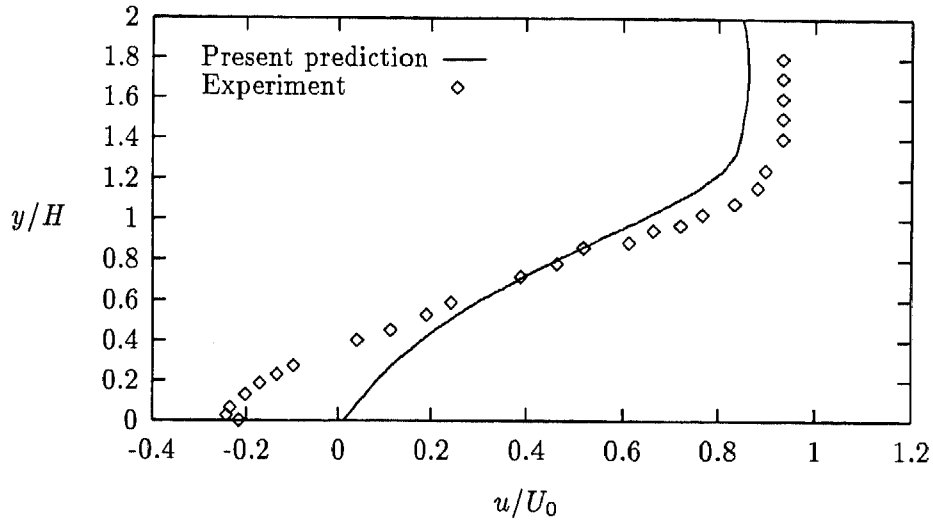

Figure 4.8: Streamwise velocity profile at $x/H = 5.33$

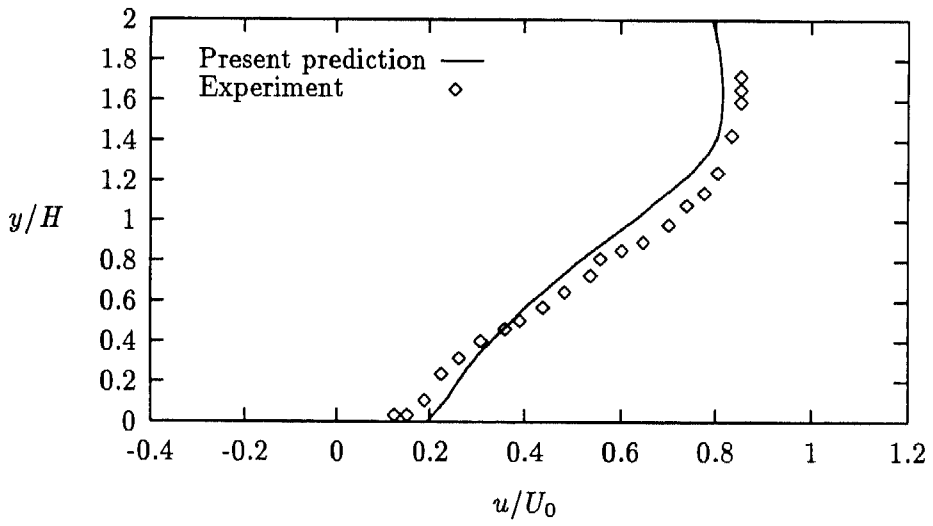

Figure 4.9: Streamwise velocity profile at $x/H = 8.00$

discrepancies are mainly due to the underprediction of the reattachment length. Furthermore, profiles of the normalized Reynolds shear stress are presented in Figures 4.11, 4.12 and 4.13. Deficiencies occur near the recirculation zone, where the shear stress peaks are underpredicted, whereas in the recovery region far downstream of the reattachment the shear stress is reasonably well predicted. The results and their deficiencies are typical of k-ε modeling. The results obtained with the present method are in very good agreement with the computations of Demirdzic (1982).

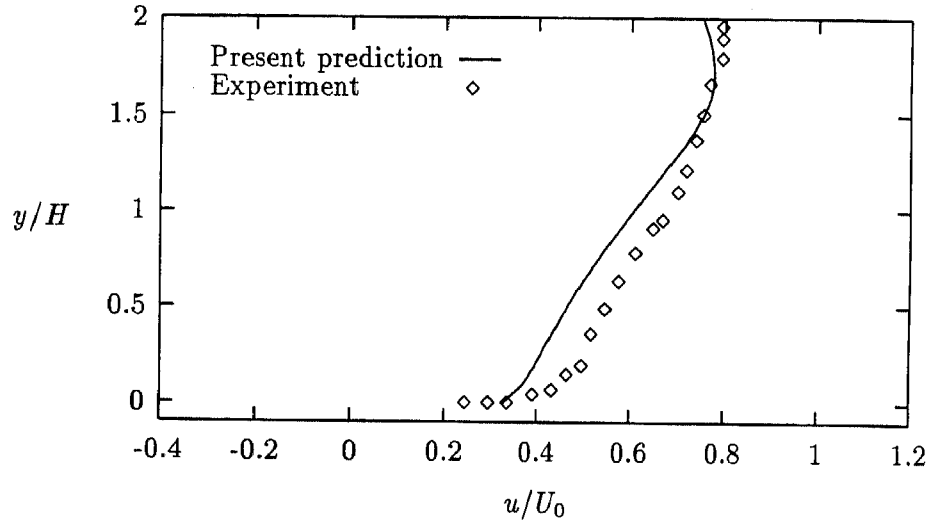

Figure 4.10: Streamwise velocity profile at $x/H = 13.33$

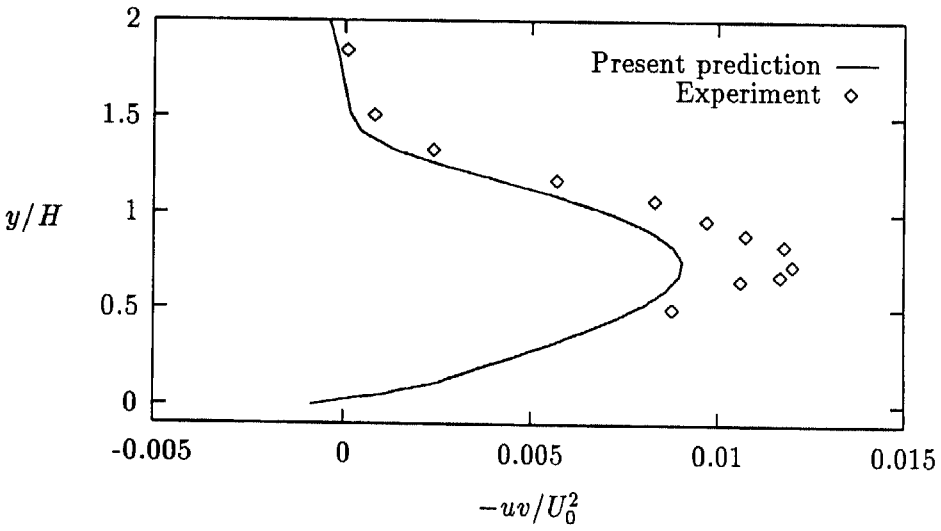

Figure 4.11: Shear stress profile at $x/H = 7.66$

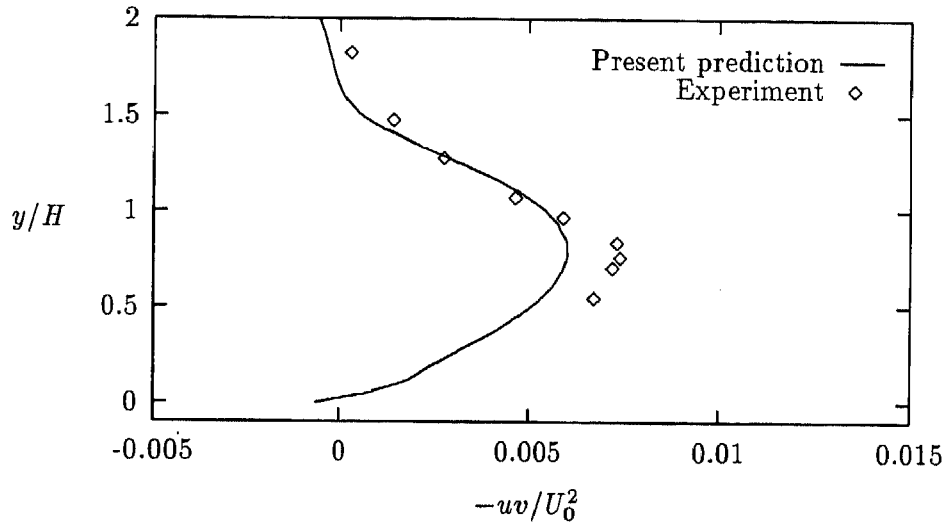

Figure 4.12: Shear stress profile at $x/H = 10.30$

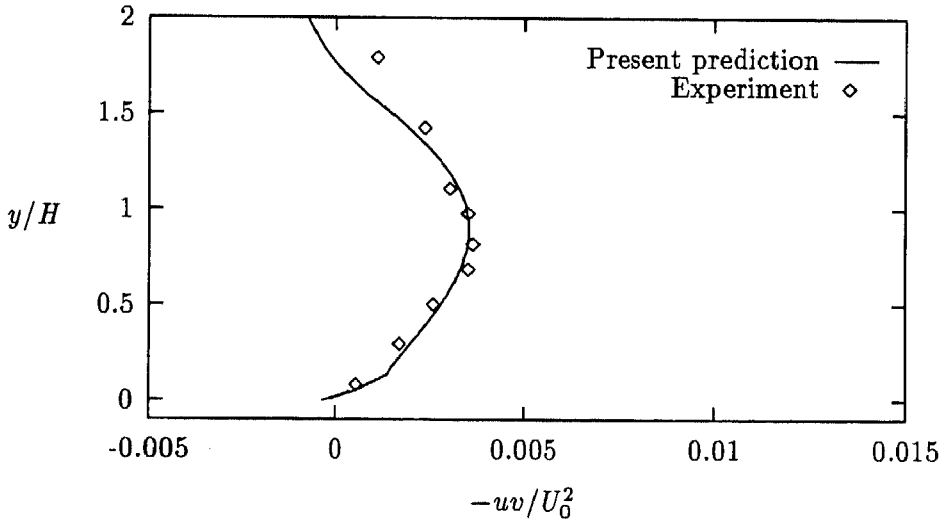

Figure 4.13: Shear stress profile at $x/H = 15.67$

From Figure 4.14 it is seen that small wiggles occur in the streamlines due to the

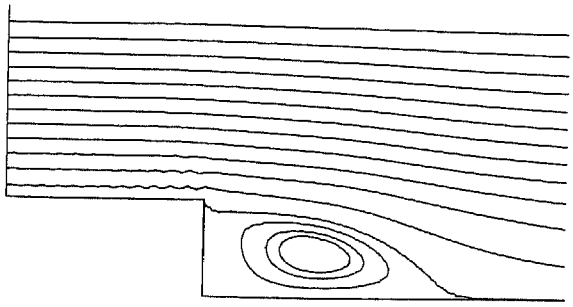

Figure 4.14: Wiggles in streamlines for turbulent flow over backward facing step

non-smoothness of the grid near the step. Although undesirable these wiggles seem to have a very small influence on the solutions, and thus are not too dramatic. As mentioned before, a multiblock approach combined with Cartesian grids is a natural approach to avoid this problem. This can be demonstrated with a computation of laminar flow over a backward facing step with $Re = 300$. It is concluded from Figures 4.15 and 4.16 that better results are obtained with the multiblock method.

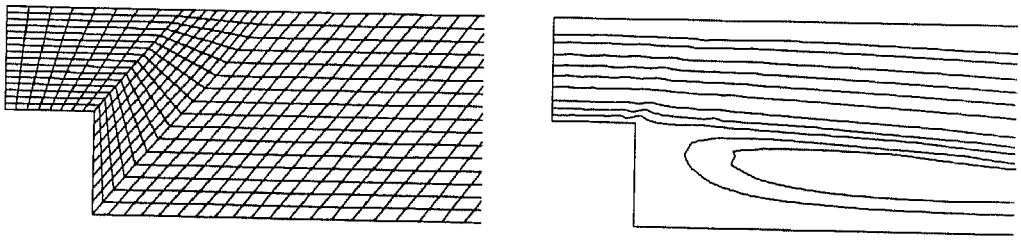

Figure 4.15: Inaccurate streamlines for $Re = 300$ with a non-smooth grid

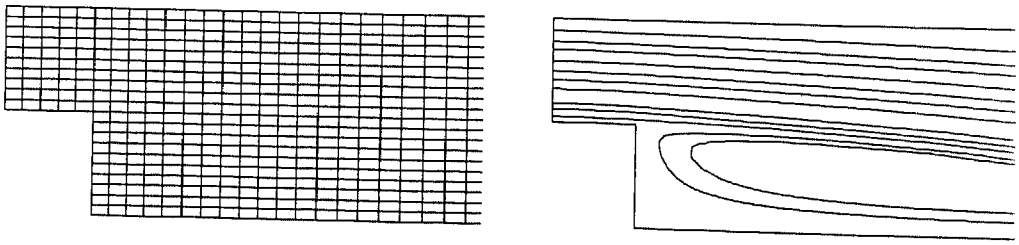

Figure 4.16: Accurate streamlines for $Re = 300$ with an orthogonal grid computed with multiblock

For more details on the multiblock method, we refer to [Brakkee and Wilders, 1994].

A way to improve the single block results would be by further smoothing of the discontinuity in the grid.

4.3 Turbulent flow through a constricted tube

The method is applied to an even more challenging turbulent flow case: turbulent flow through a tube with a sinusoidal constriction, as shown in Figure 4.17. This

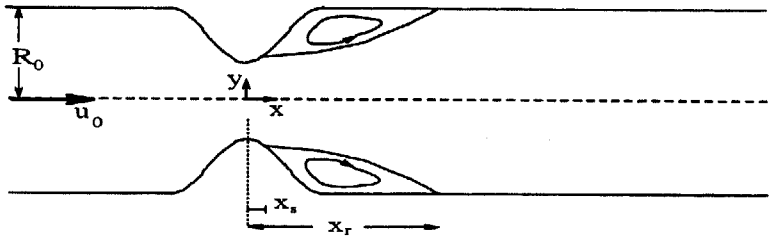

Figure 4.17: Geometry of the solution domain for the constricted tube flow

flow has been studied experimentally by Deshpande and Giddens (1980). Earlier numerical studies related to this flow type have been carried out by Rastogi (1984) and Melaaen (1991). The former used general orthogonal coordinates with a staggered grid arrangement, while the latter employed general non-orthogonal coordinates on a colocated grid.

Although the flow is axisymmetric, it was found that there is not much difference between the flow through a planar constricted duct and through a circular constricted pipe. Therefore, we consider the calculation of the flow in 2D plane constriction.

The height of the duct is 50.8 mm and the Reynolds number based on that height and the average inlet velocity is 15,000. The height and the base length of the constriction are $\frac{1}{2}R_0$ and $4R_0$, respectively, where R_0 is the half height of the duct. Due to symmetry, only the lower half of the domain needs to be considered. The inlet profiles for the velocity and turbulence quantities were specified at the plane $x = -4R_0$. Following Deshpande *et al.* (1980), at the inlet a fully-developed power-law profile ($n \approx 6.4$) is assumed for the streamwise velocity:

$$u_{in} = u_0(1 + \frac{y}{R_0})^{1/6.4} \tag{4.2}$$

where u_0 is the centerline velocity. For the turbulence quantities k and ε, the following inlet profiles are assumed:

$$k_{in} = 1.5I_T^2 u_{in}^2, \qquad \varepsilon_{in} = \frac{c_\mu^{3/4} k_{in}^{3/2}}{l} \tag{4.3}$$

Here, I_T is the turbulence intensity, taken to be 3% and l is the mixing length given by:

$$l = \min(\kappa y, 0.1R_0) \tag{4.4}$$

In addition, wall functions, symmetry and outstream conditions are imposed in the usual way.

Grid dependence tests have been performed with four grids, consisting of 50x20, 75x30, 100x60 and 150x100 cells, respectively. Figure 4.18 shows the 50x20 grid. The test focussed primarily on the separation and reattachment lengths. The computed separation and reattachment lengths are presented, together with the measurements

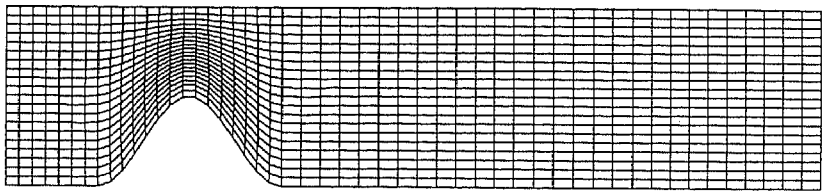

Figure 4.18: A typical grid for the constricted tube flow (50x20 cells)

	Separation x_s/R_0	Reattachment x_r/R_0
Experiment	0.5	4.0
Rastogi, 41 × 21	1.2	2.4
Melaaen, 52 × 22	0.89	3.02
Present, 50 × 20	1.06	3.07
Present, 75 × 30	0.93	3.10
Present, 100 × 60	0.64	3.36
Present, 150 × 100	0.56	3.50

Table 4.1: Variation of separation and reattachment lengths with different grids

and earlier calculations of Rastogi and Melaaen in Table 4.1. From this Table it is seen that calculated separation length is overpredicted, while the reattachment length is underpredicted. Furthermore, the agreement between the present results and the results of Melaaen corresponding to grid resolution of the same order can be said to be satisfactory. It should be noted that Rastogi used the hybrid scheme and Melaaen used the power law scheme of Patankar (1980) for solving both the momentum and turbulence equations. Moreover, Melaaen also employed a second-order upwind scheme [Peric, 1985] for solving the momentum equations while the power law scheme is still used for solving turbulence equations. In that case, on the 52x22 grid the calculated separation and reattachment lengths are $x_s/R_0 = 0.56$ and $x_r/R_0 = 4.07$, respectively, as has been reported in [Melaaen, 1991].

The predicted lengths of separation and reattachment decrease and increase, respectively, with grid refinement approaching the experimental lengths. Although the reattachment and separation lengths still show some variation between two finest grids, further mesh refinement was not perform because of prohibitive demands for computing time and to avoid that the first y^+ point is too close to the wall. Hence, all subsequent computations were done with a 150x100 grid. Figure 4.19 presents typical features of this flow, including streamlines and contours of isobars and turbulence quantities.

Figures 4.20, 4.21 and 4.22 show the streamwise velocity predictions at different stations. The calculation is seen to yield good agreement with the measurements, except for the station $x/R_0 = 2.0$, although the profiles shapes are the same. This

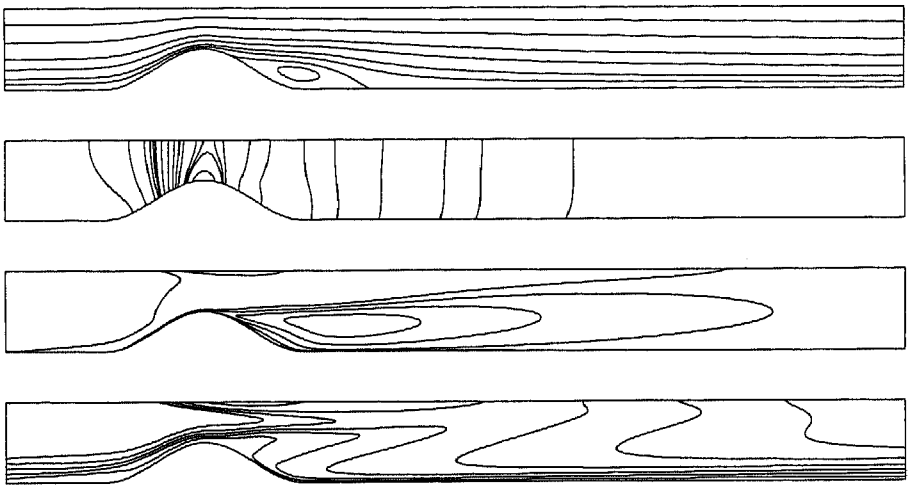

Figure 4.19: Typical flow pattern for contricted tube: streamlines, isobars, turbulence intensity and length scales, respectively

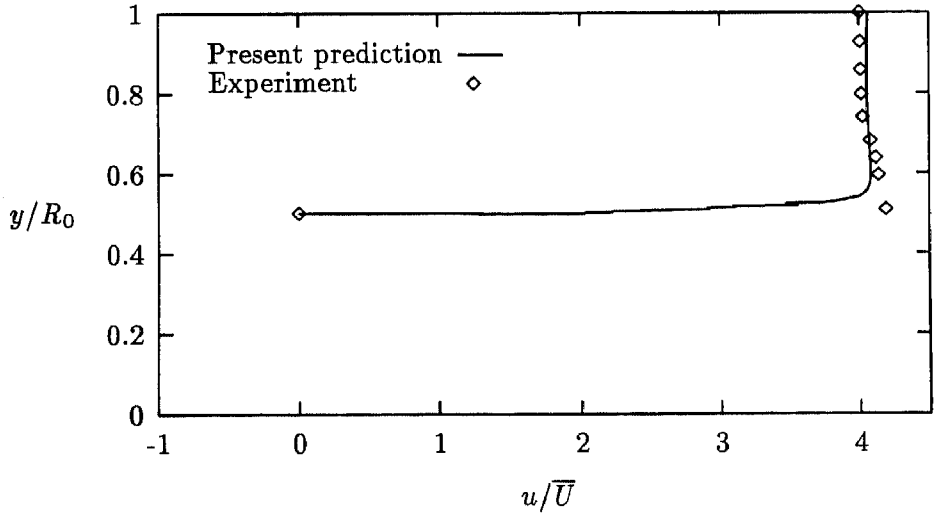

Figure 4.20: Streamwise velocity profile at $x/R_0 = 0.0$

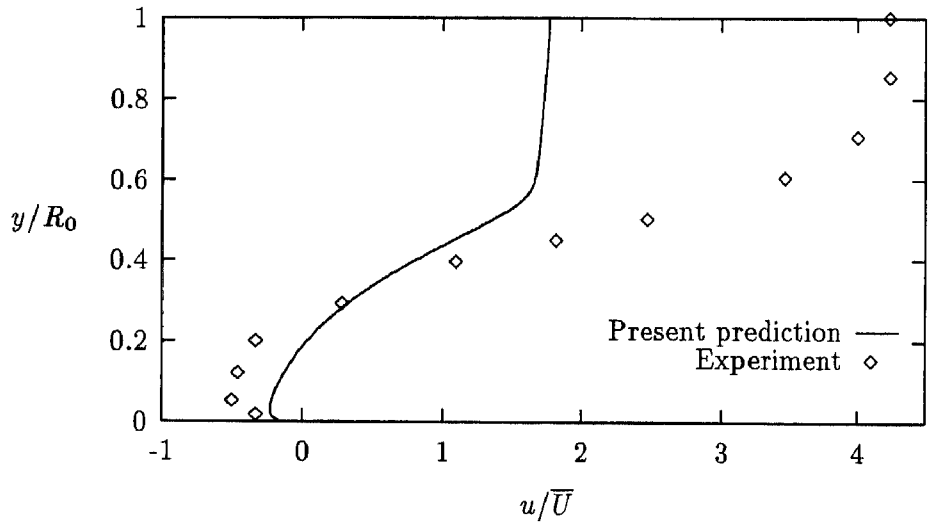

Figure 4.21: Streamwise velocity profile at $x/R_0 = 2.0$

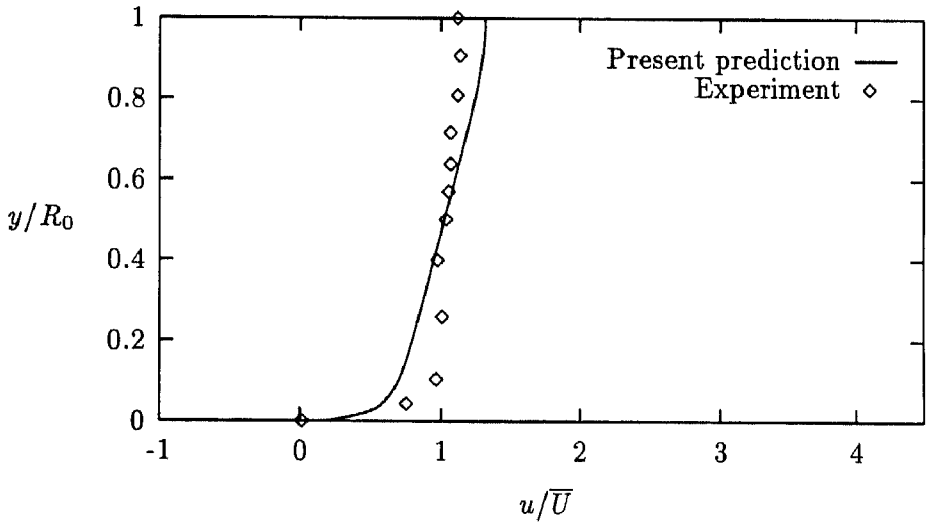

Figure 4.22: Streamwise velocity profile at $x/R_0 = 11.0$

is not surprising, because it is well-known that the k-ε model does not scale well in and around the recirculation zone. Furthermore, both the present method and the methods of Rastogi and Melaaen produce very similar velocity profiles.

Figure 4.23 shows a comparison of the predicted wall static pressure with the

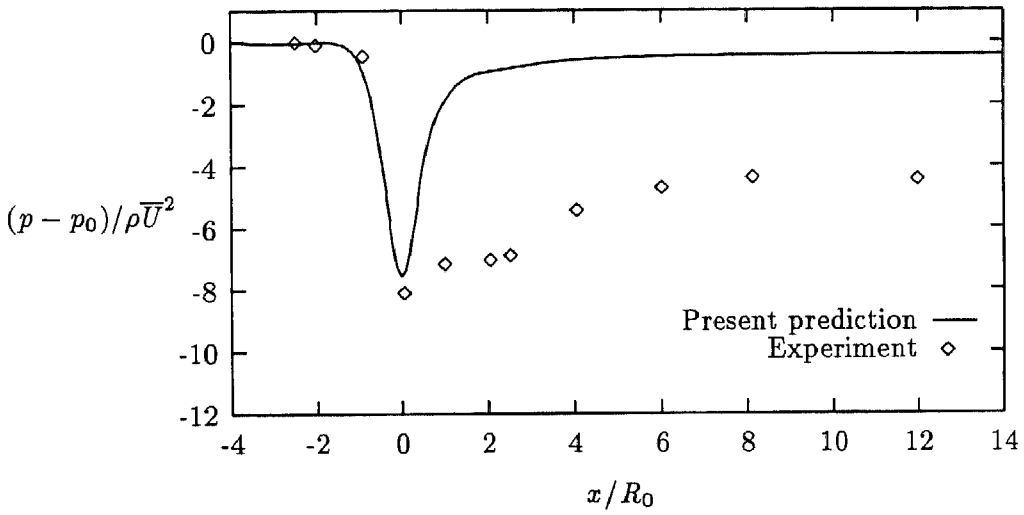

Figure 4.23: Wall static pressure distribution

measurements. In the acceleration region, where a steep decline of the pressure occurs, the pressure is well predicted. In the deceleration part, however, the present method gives an excessive pressure recovery. The same conclusion is drawn by both Rastogi and Melaaen.

Finally, the profile of the centerline turbulence intensity is compared with measurements in Figure 4.24. The comparison indicates that the predicted turbulence

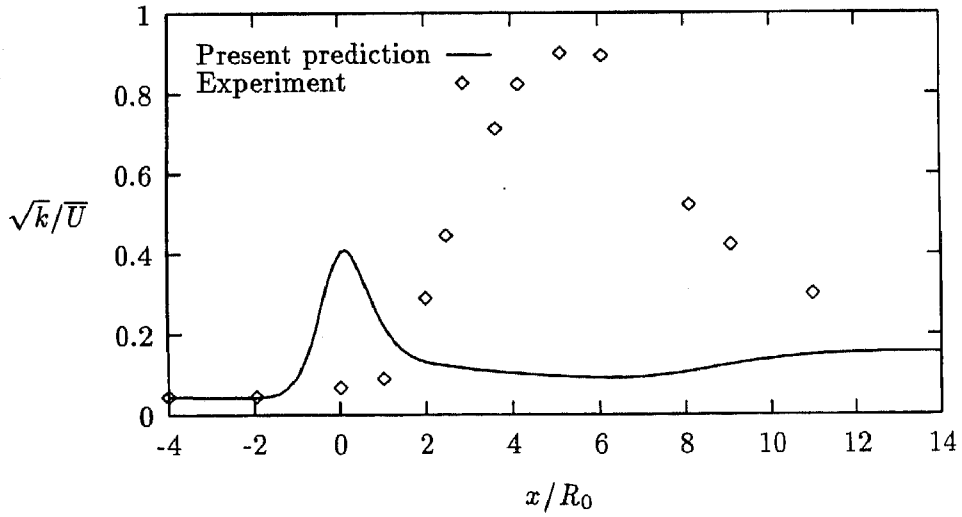

Figure 4.24: Turbulence intensity distribution along the centerline

intensity increases too early, and the measured one increases after separation occurs,

whereas the computed one decreases there. Moreover, the peak of the predicted turbulence intensity is too low. Again, it is believed that the errors lie in the k-ε model. Although the agreement between the predicted and measured turbulence intensity is not satisfactory, there is a qualitative accordance with the computed results of Rastogi.

4.4 Turbulent flow through an U-bend

This section is concerned with the application of the present method to the prediction of flow through a sharp two-dimensional U-bend as shown in Figure 4.25. Such a flow

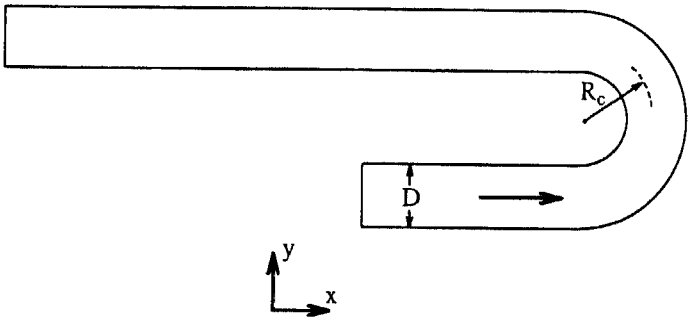

Figure 4.25: U-bend geometry

occurs for example in cooling passages within gas-turbine blades. Earlier numerical studies were made by e.g. Choi *et al.* (1989) and Bo and Iacovides (1993). We compare our results with numerical results from Bo *et al.* and experimental data taken from [Bo and Iacovides, 1993].

The bend geometry considered here has a curvature ratio $R_c/D = 0.65$, which causes separation. Here D is the width of the duct. The Reynolds number based on the duct width and the centerline inflow velocity U_c is 100,000. The inflow boundary is located at three duct widths upstream of the bend, whereas the outflow is specified at eight duct widths downstream of the bend. At smooth walls, the wall functions are applied. The streamwise velocity at inflow is described according to the power-law profile with $n = 7$, whereas k and ε are obtained from the formula (4.3). Here, the turbulence intensity is taken to be 6% (in accordance with the experiment) and $l = \min(\kappa y, 0.5D)$.

First, computations were performed to examine the grid dependence of the solutions. To this end, three grids of 50x30, 90x50 and 150x90 cells were used. Figures 4.26 gives the 50x30 grid. The grid is non-orthogonal. Test results are shown in Figure 4.27 and 4.28 for the streamwise velocity and the turbulence intensity at $1D$ downstream of the bend. It can be seen that unlike the turbulence intensity the velocity is already grid independent on the 90x50 grid. Further grid refinement was not pursued, because it is believed that it gives smaller differences than those provoked by the k-ε model. Hence, the calculations for the 150x90 grid are considered.

Contour plots of streamlines, isobars, turbulence intensity and length scales are shown in Figures 4.29, 4.30, 4.31 and 4.32. The streamlines show the expected

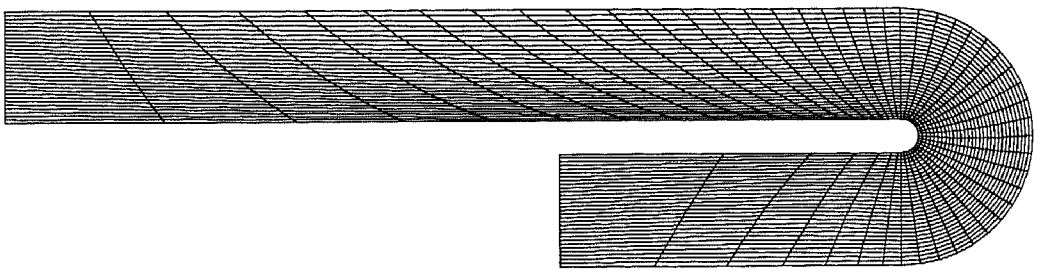

Figure 4.26: A typical grid, 50x30 cells

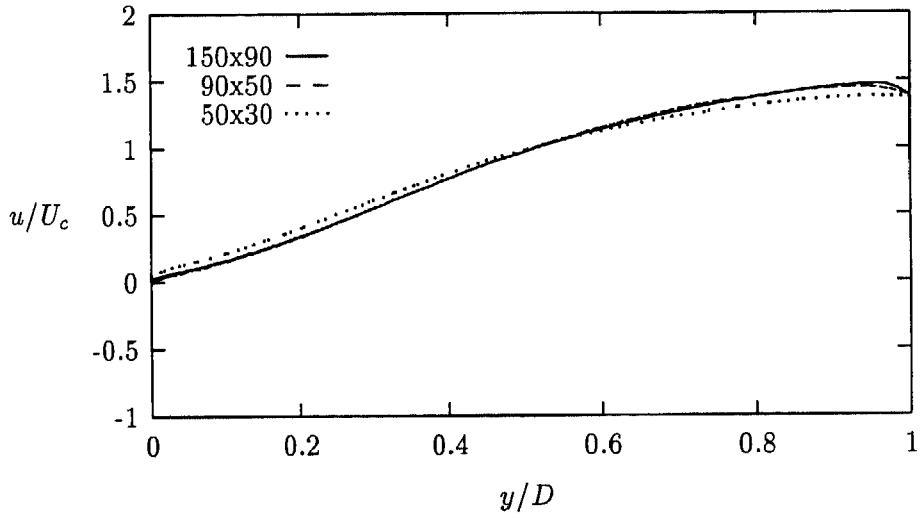

Figure 4.27: Grid refinement test for U-bend (velocity profiles)

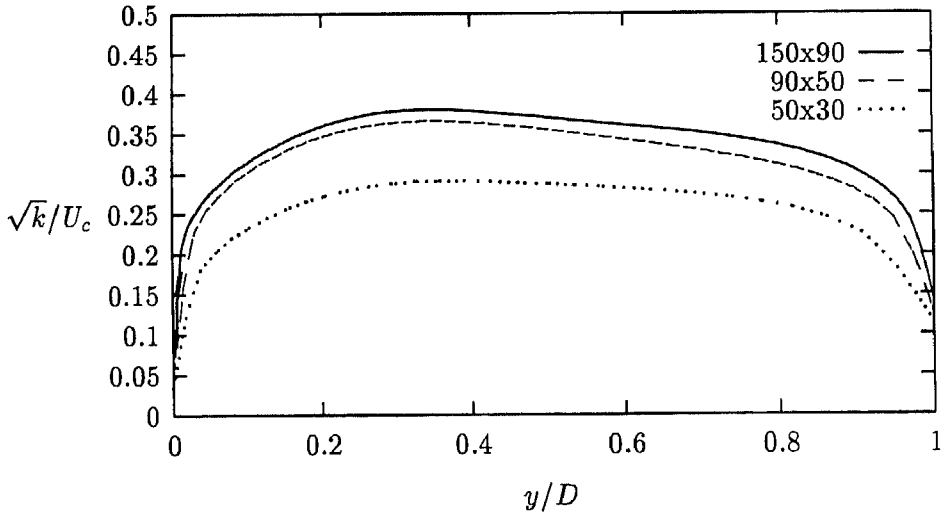

Figure 4.28: Grid refinement test for U-bend (turbulence intensity profiles)

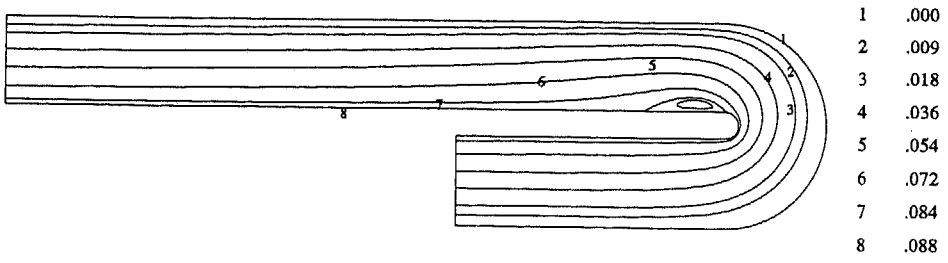

Figure 4.29: Streamlines for flow through U-bend

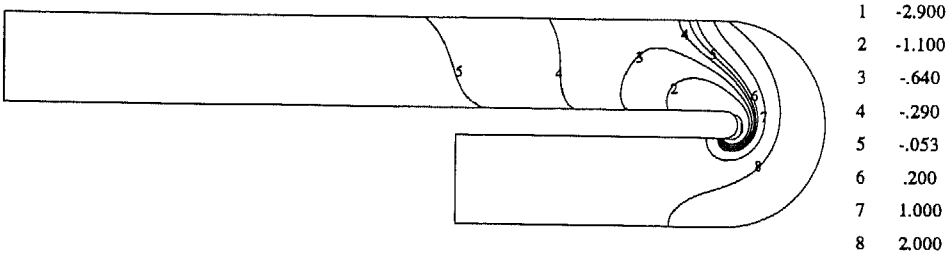

Figure 4.30: Isobars for flow through U-bend

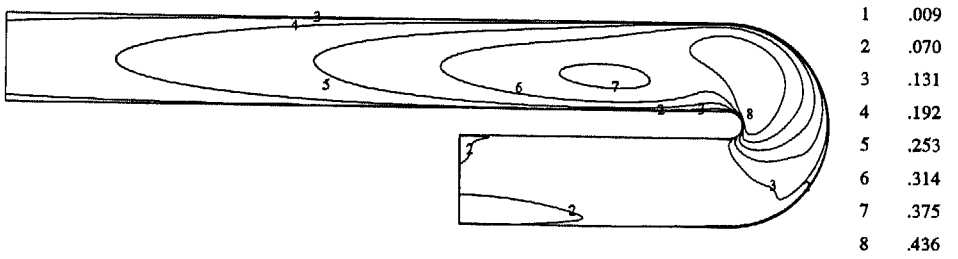

Figure 4.31: Turbulence intensity $\sqrt{k}/U_c$ for flow through U-bend

behaviour and also indicate that the length of the recirculation zone is about one duct width. The isobars shows also the qualitatively correct behaviour: high pressure in the impingement region, low pressure in the recirculation region and pressure recovery after separation. Also expected is the build up of turbulence intensity from the walls, especially in the impingement region.

The results of the computations are compared with the predictions obtained by Bo *et al.* (1993) and the measurements taken from [Bo and Iacovides, 1993]. Bo *et al.* performed 3D calculations on orthogonal grids. Present results will be compared with their results at the symmetry plane. They used the standard k-ε model, whereas a k-l model is used in the near-wall regions instead of wall functions. Furthermore, they employed two convection schemes: the hybrid central/upwind scheme and a blended scheme, called LODA [Zhou and Leschziner, 1988], in which the convective transport is approximated by a combination of the well-known QUICK and first

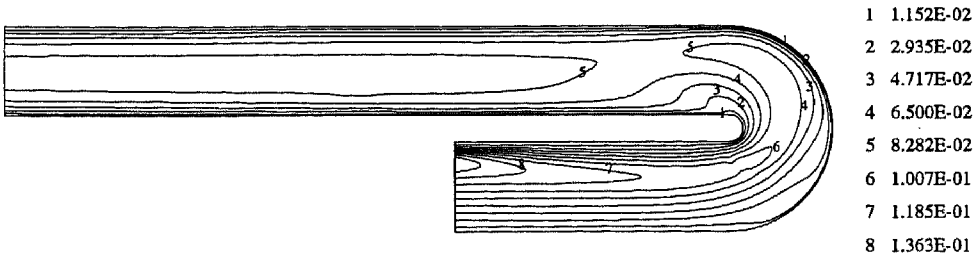

Figure 4.32: Length scales $c_\mu k^{\frac{3}{2}}/\varepsilon D$ for flow through U-bend

order upwind schemes. Blending of these two schemes is determined by a so-called blending factor which is generally unknown. Hence, an iterative procedure is needed in order to determine the blending factor. Another disadvantage of this blending technique is that several measures are introduced to improve numerical stability and to prevent negative values of k and ε [Bo *et al.*, 1993]. Therefore, one may expected that this blending technique is very costly.

In Figures 4.33, 4.34, 4.35 and 4.36 the streamwise velocity and the turbulence

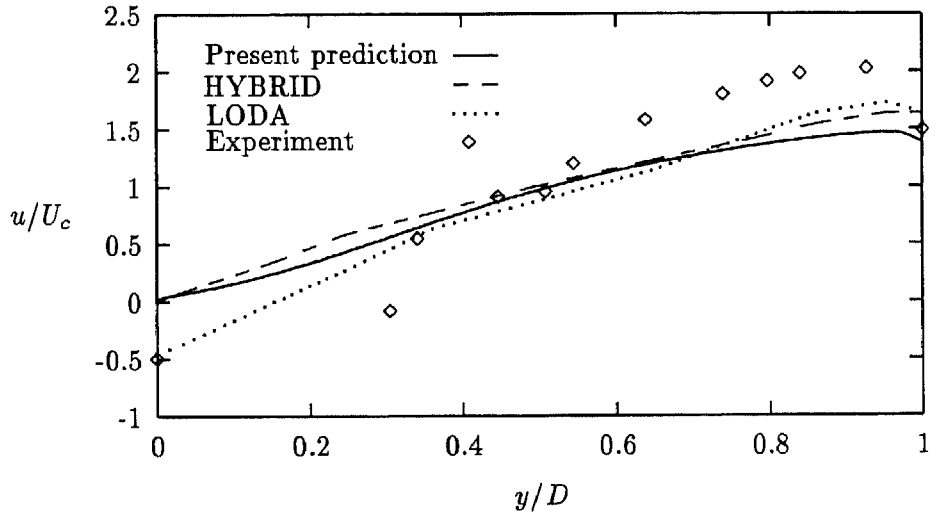

Figure 4.33: Streamwise velocity at $1D$ downstream of the bend

intensity profiles are presented at $1D$ and $3D$ downstream of the bend. "LODA" means that the LODA scheme is employed on both momentum and turbulence equations on a 133x67x35 grid, whereas "HYBRID" denotes the application of the hybrid scheme on both momentum and turbulence equations on a 177x77x35 grid. With respect to our computations, the following conclusions may be drawn. At $1D$ downstream of the bend, the velocity is reasonably well predicted, although the recirculation length is underpredicted. There is no qualitative accordance between the prediction and measurements of the streamwise velocity at $3D$ downstream of the bend. Furthermore, at $1D$ downstream of the bend, the turbulence intensity near the inner side of the duct is predicted very well, while the turbulence level near the outer wall is overestimated. Finally, at $3D$ downstream of the bend, the

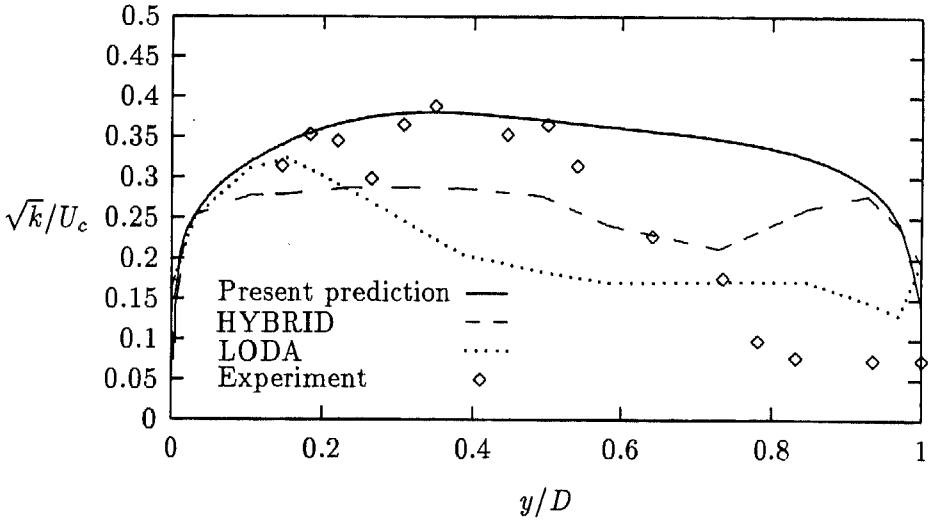

Figure 4.34: Turbulence intensity at $1D$ downstream of the bend

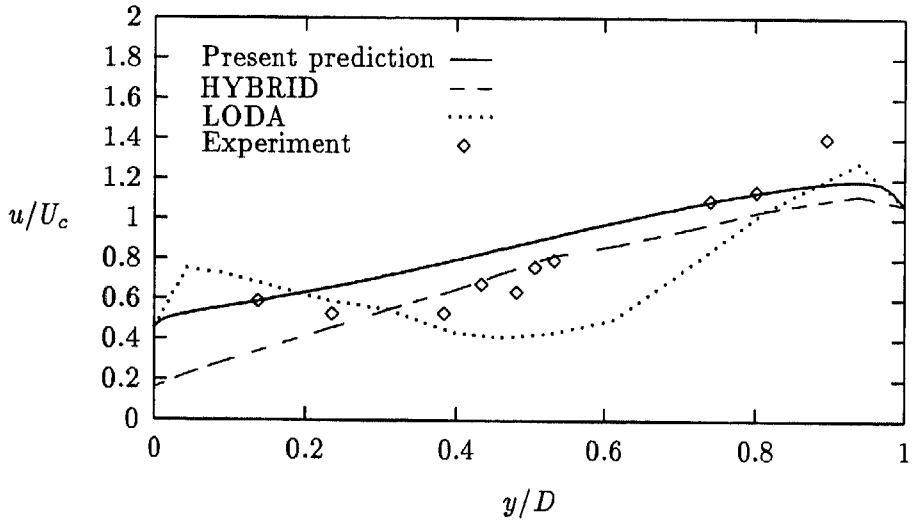

Figure 4.35: Streamwise velocity at $3D$ downstream of the bend

turbulence intensity is somewhat lower than the measured one.

Overall, the standard k-ε model does not produce accurate solutions, because this model is not capable of predicting effects of curvature on the turbulence. But there is qualitative agreement between computation and experiment, and satisfactory agreement between the HYBRID scheme of Bo *et al.* and the present computations.

5 Conclusions

An invariant finite volume discretization in general coordinates of the Reynolds-averaged Navier-Stokes equations with the standard k-ε model on staggered grids has been presented. Central differencing is used for convection of momentum, whereas

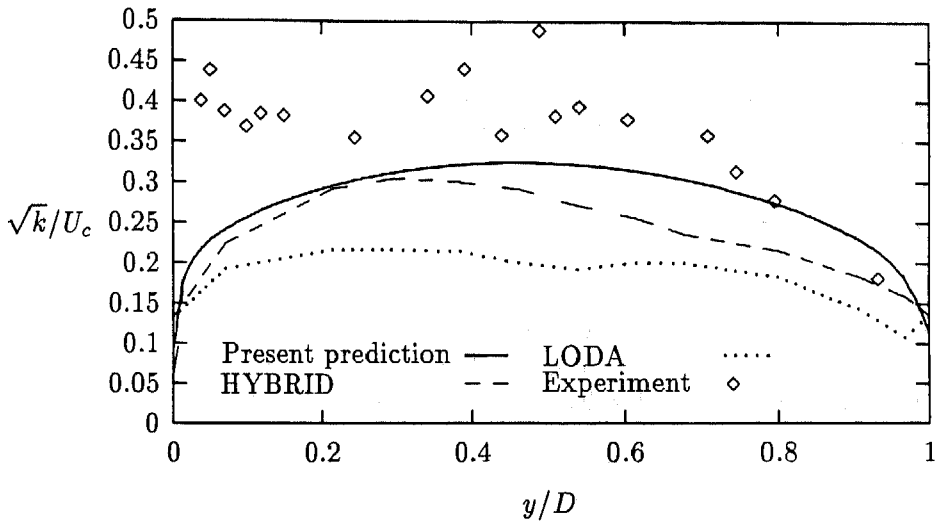

Figure 4.36: Turbulence intensity at $3D$ downstream of the bend

the hybrid central/upwind scheme is employed for convection of k and ε, to prevent negative values of k and ε. The diffusion terms are approximated with central differences. The mixed derivatives in these terms are treated implicitly. The present method was applied to several 2D turbulent flows in arbitrarily shaped domains. The agreement between the results of the computations and the experimental data or the predictions obtained by other methods was found to be satisfactory, within the limitations of the standard k-ε model employed. The calculation of the backward facing step flow has demonstrated that the present discretization is not accurate enough on very non-smooth grids. It turns out that a multiblock method is more suitable to avoid such inaccuracies.

References

1. R. Aris. *Vectors, tensors and the basic equations of fluid mechanics.* Prentice-Hall Inc., Englewood Cliffs, N.J., 1962.

2. W.D. Baines and D.J. Knapp. Wind driven water currents. *J. Hydraulics Division ASCE*, 91:295–321, 1965.

3. T. Bo and H. Iacovides. The discretization of the turbulence transport equations in the prediction of flow and heat transfer through a sharp U-bend. In C. Taylor, editor, *Proc. Eighth Int. Conf. on Numer. Meth. Laminar and Turbulent Flow*, pages 351–362, Pineridge Press, Swansea, U.K., 1993.

4. M. Braaten and W. Shyy. A study of recirculating flow computation using body-fitted coordinates: consistency aspects and mesh skewness. *Numer. Heat Transfer*, 9:559–574, 1986.

5. E. Brakkee and P. Wilders. A domain decomposition method for the advection-diffusion equation. Report 94-08, Delft University of Technology, Faculty of Technical Mathematics and Informatics, Delft, The Netherlands, 1994.

6. H.C. Chen and V.C. Patel. The flow around wing-body junctions. In *Fourth Symp. on Numer. and Phys. Aspects of Aerod. Fl.*, pages 1–15, Long Beach, USA, 1989.

7. H.C. Chen, V.C. Patel, and S. Ju. Solutions of Reynolds-averaged Navier-Stokes equations for three-dimensional incompressible flows. *J. Comput. Phys.*, 88:305–336, 1990.

8. N-H. Cho and C.A.J. Fletcher. Computation of turbulent conical diffuser flows using a non-orthogonal grid system. *Comput. Fluids*, 19:347–361, 1991.

9. Y.D. Choi, H. Iacovides, and B.E. Launder. Numerical computation of turbulent flow in a square-sectioned 180 deg bend. *ASME J. Fluids Engng.*, 111:59–68, 1989.

10. P.J. Coelho and J.C.F. Pereira. Finite volume computation of the turbulent flow over a hill employing 2D or 3D non-orthogonal collocated grid systems. *Int. J. Numer. Meth. Fluids*, 14:423–441, 1992.

11. I. Demirdzic, A.D. Gosman, R.I. Issa, and M. Perić. A calculation procedure for turbulent flow in complex geometries. *Comput. Fluids*, 15:251–273, 1987.

12. I.A. Demirdzic. *A finite volume method for computation of fluid flow in complex geometries.* Ph.D. thesis, University of London, 1982.

13. G.B. Deng. Numerical simulation of incompressible turbulent appendage-flat plate junction flows. In C. Taylor, W.G. Habashi, and M.M. Hafez, editors, *Proc. Sixth Int. Conf. on Numer. Meth. Laminar and Turbulent Flow*, pages 793–803, Pineridge Press, Swansea, U.K., 1989.

14. M.D. Deshpande and D.P. Giddens. Turbulence measurements in a constricted tube. *J. Fluid Mech.*, 97:65–89, 1980.

15. M.A. Habib and J.H. Whitelaw. The calculation of turbulent flow in wide-angle diffusers. *Numer. Heat Transfer*, 5:145–164, 1982.

16. R.I. Issa and P.J. Oliveira. Numerical prediction of phase separation in two-phase flow through T-junctions. *Comput. Fluids*, 23:347–372, 1994.

17. J.J.I.M. Van Kan. A second-order accurate pressure correction method for viscous incompressible flow. *SIAM J. Sci. Stat. Comput.*, 7:870–891, 1986.

18. J. Kim, S.J. Kline, and J.P. Johnston. Investigation of a reattaching turbulent shear layer: flow over a backward-facing step. *ASME J. Fluids Engng.*, 102:302–308, 1980.

19. S. Koshizuka and Y. Oka. A calculation procedure of coordinate-free Navier-Stokes equations on boundary-fitted grids. In C. Taylor, J.H. Chin, and G.M. Homsy, editors, *Proc. Seventh Int. Conf. on Numer. Meth. Laminar and Turbulent Flow*, pages 1474–1484, Pineridge Press, Swansea, U.K., 1991.

20. D. Kwak, J.L.C. Chang, S.P. Shanks, and S.R. Chakravarthy. A three-dimensional incompressible Navier-Stokes flow solver using primitive variables. *AIAA J.*, 24:390–396, 1986.

21. B.E. Launder and D.B. Spalding. The numerical computation of turbulent flows. *Comput. Meth. Appl. Mech. Engng.*, 3:269–289, 1974.

22. F-S. Lien and M.A. Leschziner. Multigrid convergence acceleration for complex flow including turbulence. In W. Hackbush and U. Trottenberg, editors, *Multigrid Methods III*, volume 98, pages 277–288, Birkhäuser, Basel, 1991.

23. S. Majumdar and W. Rodi. Three-dimensional computation of flow past cylindrical structures and model cooling towers. *Building and Environment*, 24:3–22, 1989.

24. M.C. Melaaen. Analysis of fluid flow in constricted tubes and ducts using body-fitted non-staggered grids. *Int. J. Numer. Meth. Fluids*, 15:895–923, 1991.

25. V. Michelassi and F. Martelli. Efficient solution of turbulent incompressible separated flows. In P. Wesseling, editor, *Proc. Eighth GAMM Conf. on Numer. Meth. Fluid Mech.*, pages 373–390, Vieweg, Braunschweig/Wiesbaden, 1990. Notes on Numerical Fluid Mechanics 29.

26. A.E. Mynett, P. Wesseling, A. Segal, and C.G.M. Kassels. The ISNaS incompressible Navier-Stokes solver: invariant discretization. *Appl. Sci. Res.*, 48:175–191, 1991.

27. M. Nallasamy. Turbulence models and their applications to the prediction of internal flows: a review. *Comput. Fluids*, 15:151–194, 1987.

28. S.V. Patankar. *Numerical heat transfer and fluid flow.* McGraw-Hill, New York, 1980.

29. M. Perić. *Finite volume method for the prediction of three-dimensional fluid flow in complex ducts.* Ph.D. thesis, Imperial College, London, 1985.

30. J. Piquet and P. Queutey. Computation of the viscous flow past a prolate spheroid at incidence. In P. Wesseling, editor, *Proc. Eighth GAMM Conf. on Numer. Meth. Fluid Mech.*, pages 464–473, Vieweg, Braunschweig/Wiesbaden, 1990. Notes on Numerical Fluid Mechanics 29.

31. S.B. Pope. The calculation of turbulent recirculating flows in general orthogonal coordinates. *J. Comput. Phys.*, 26:197–217, 1978.

32. C.W. Rapley. Turbulent flow in a duct with cusped corners. *Int. J. Numer. Meth. Fluids*, 5:155–167, 1985.

33. A.K. Rastogi. Hydrodynamics in tubes pertubed by curvilinear obstructions. *ASME J. Fluids Engng.*, 106:262–269, 1984.

34. C.M. Rhie and W.L. Chow. Numerical study of the turbulent flow past an airfoil with trailing edge separation. *AIAA J.*, 21:1525–1532, 1983.

35. W. Rodi. *Turbulence models and their application in hydraulics - A state of the art review.* International Association of Hydraulic Research, Delft, The Netherlands, 1984.

36. H. Rolfes, J.A. Visser, and A. Bekker. Simulation of wind flow over arbitrary shaped buildings. In C. Taylor, editor, *Proc. Eighth Int. Conf. on Numer. Meth. Laminar and Turbulent Flow*, pages 643–654, Pineridge Press, Swansea, U.K., 1993.

37. Y. Saad and M.H. Schultz. GMRES: a generalized minimal residual algorithm for solving non symmetric linear systems. *SIAM J. Sci. Stat. Comput.*, 7:856–869, 1986.

38. A. Segal, P. Wesseling, J. van Kan, C.W. Oosterlee, and K. Kassels. Invariant discretization of the incompressible Navier-Stokes equations in boundary fitted co-ordinates. *Int. J. Numer. Meth. Fluids*, 15:411–426, 1992.

39. G. Segal, K. Vuik, and K. Kassels. On the implementation of symmetric and antisymmetric periodic boundary conditions for incompressible flow. *Int. J. Numer. Meth. Fluids.* To appear.

40. D.B. Spalding. A novel finite-difference formulation for differential expressions involving both first and second derivatives. *Int. J. Numer. Meth. Engng.*, 4:551–559, 1972.

41. F. Stern, S.Y. Yoo, and V.C. Patel. Interactive and large-domain solutions of higher-order viscous-flow equations. *AIAA J.*, 26:1052–1060, 1988.

42. H.L. Stone. Iterative solution of implicit approximations of multidimensional partial differential equations. *SIAM J. Numer. Anal.*, 5:530–558, 1968.

43. S. Thangam and C.G. Speziale. Turbulent separated flow past a backward-facing step: a critical evaluation of two-equation turbulence models. ICASE Report 91-23, Institute for Computer Applications in Science and Engineering, NASA Langley Research Center, Hampton, Virginia, 1991.

44. C. Vuik. Solution of the discretized incompressible Navier-Stokes equations with the GMRES method. *Int. J. Numer. Meth. Fluids*, 16:507–523, 1993.

45. P. Wesseling, A. Segal, J.J.I.M. van Kan, C.W. Oosterlee, and C.G.M. Kassels. Finite volume discretization of the incompressible Navier-Stokes equations in general coordinates on staggered grids. *Comput. Fluid Dyn. J.*, 1:27–33, 1992.

46. Z.G. Xu, D.H.T. Gotham, and M.W. Collins. Numerical modelling of three-dimensional turbulent flow in packaged air-conditioning units with inclined heat exchangers. In C. Taylor, editor, *Proc. Eighth Int. Conf. on Numer. Meth. Laminar and Turbulent Flow*, pages 328–337, Pineridge Press, Swansea, U.K., 1993.

47. C-N. Yung, T.G. Keith Jr., and K.J. de Witt. Numerical simulation of axisymmetric turbulent flow in combustors and diffusers. *Int. J. Numer. Meth. Fluids*, 9:167–183, 1989.

48. H. Zhou and M.A. Leschziner. A local oscillation-damping algorithm for higher order convection schemes. *Comput. Meth. Appl. Mech. Engng.*, 67:355–366, 1988.

49. J. Zhu and W. Rodi. Computation of axisymmetric confined jets in a diffuser. *Int. J. Numer. Meth. Fluids*, 14:241–251, 1992.

50. M. Zijlema. Finite volume discretization of the k-ε turbulence model in general coordinates. Report 93-90, Delft University of Technology, Faculty of Technical Mathematics and Informatics, Delft, The Netherlands, 1993.

The following reports have appeared in this series:

94-12	Florin Dan Barb, Vlad Ionescu and Willem de Koning	A Popov theory based approach to digital H^∞-conttol with measurement-feedback for Pritchard-Salamon systems
94-13	F.A. Lootsma	The multiplicative AHP, SMART and ELECTRE in a common context
94-14	Bastian Blonk, Gérard C. Herman, Guy G. Drijkoningen	As elastodynamic inverse scattering method for removing scattered surface waves from field data
94-15	P. van Beek, R.R.P. van Nooyen and P. Wesseling	Accurate discretization of gradients on non-uniform curvilinear staggered grids
94-16	Maurice Dohmen	Constraint techniques in interactive feature modeling
94-17	L.A. de Looff en E.W. Berghout	Vormen van onderzoek naar informatievoorziening in organisaties Geëffende paden bestaan niet
94-18	Henk J. Prins and Aad J. Hermans	Time domain calculations of the second-order drift force on a floating three-dimensional object in current and waves
94-19	W.A.J. Luxemburg, B. de Pagter, A.R. Schep	Diagonals of the powers of an operator on a Banach lattice
94-20	Ph. Clément, R. Hagmeijer, G. Sweers	On the invertibility of mappings arising in 2D grid generation problems
94-21	Florin Dan Barb en Willem de Koning	Het vaste-orde eindig-dimensionale dynamische digitale compensatieprobleem voor Pritchard-Salamon systemen
94-22	Serguei Foss, Gerard Hooghiemstra, Michael Keane	On a problem of Jon Wellner
94-23	T. Illés and G. Kassay	Farkas type theorems for generalized convexities
94-24	M. Zijlema, A. Segal and P. Wesseling	Finite volume computation of 2D incompressible turbulent flows in general coordinates on staggered grids

Copies of these reports may be obtained from the bureau of the Faculty of Technical Mathematics and Informatics, Julianalaan 132, 2628 BL DELFT, phone 015-784568.
A selection of these reports is available in PostScript form at the Faculty's anonymous ftp-site. They are located in the directory /pub/publications/tech-reports at ftp.twi.tudelft.nl.